Article

Record Low Arctic Stratospheric Ozone in Spring 2020: Measurements of Ground-Based Differential Optical Absorption Spectroscopy in Ny-Ålesund during 2017–2021

Qidi Li [1,2], Yuhan Luo [1,*], Yuanyuan Qian [1,2], Ke Dou [1], Fuqi Si [1] and Wenqing Liu [1]

1 Key Laboratory of Environmental Optics and Technology, Anhui Institute of Optics and Fine Mechanics, Hefei Institutes of Physical Science, Chinese Academy of Sciences, Hefei 230031, China; qidili@mail.ustc.edu.cn (Q.L.); yyqian@aiofm.ac.cn (Y.Q.); douke@aiofm.ac.cn (K.D.); sifuqi@aiofm.ac.cn (F.S.); wqliu@aiofm.ac.cn (W.L.)
2 University of Science and Technology of China, Hefei 230026, China
* Correspondence: yhluo@aiofm.ac.cn

Abstract: The Arctic stratospheric ozone depletion event in spring 2020 was the most severe compared with previous years. We retrieved the critical indicator ozone vertical column density (VCD) using zenith scattered light differential optical absorption spectroscopy (ZSL-DOAS) from March 2017 to September 2021 in Ny-Ålesund, Svalbard, Norway. The average ozone VCD over Ny-Ålesund between 18 March and 18 April 2020 was approximately 274.8 Dobson units (DU), which was only 64.7 ± 0.1% of that recorded in other years (2017, 2018, 2019, and 2021). The daily peak difference was 195.7 DU during this period. The retrieved daily averages of ozone VCDs were compared with satellite observations from the Global Ozone Monitoring Experiment-2 (GOME-2), a Brewer spectrophotometer, and a Système d'Analyze par Observation Zénithale (SAOZ) spectrometer at Ny-Ålesund. As determined using the empirical cumulative density function, ozone VCDs from the ZSL-DOAS dataset were strongly correlated with data from the GOME-2 and SAOZ at lower and higher values, and ozone VCDs from the Brewer instrument were overestimated. The resulting Pearson correlation coefficients were relatively high at 0.97, 0.87, and 0.91, respectively. In addition, the relative deviations were 2.3%, 3.1%, and 3.5%, respectively. Sounding and ERA5 data indicated that severe ozone depletion occurred between mid-March and mid-April 2020 in the 16–20 km altitude range over Ny-Ålesund, which was strongly associated with the overall persistently low temperatures in the winter of 2019/2020. Using ZSL-DOAS observations, we obtained ozone VCDs and provided evidence for the unprecedented ozone depletion during the Arctic spring of 2020. This is essential for the study of polar ozone changes and their effect on climate change and ecological conditions.

Keywords: Arctic ozone depletion; differential optical absorption spectroscopy; vertical column density; low temperature

1. Introduction

Stratospheric ozone is essential for human health, surface ecosystems, and the climate in general because it absorbs ultraviolet (UV) solar radiation and converts it into thermal energy [1,2]. The characteristic absorption bands of stratospheric ozone are mainly located in the Hartley and Huggins zones of the UV region and the Chappuis zone of the visible spectrum; thereby absorbing almost all UV-C (i.e., wavelengths < 280 nm) and some UV-B (i.e., wavelengths ranging between 280 and 315 nm) radiation [3–5]. Since the late 1970s, the Antarctic stratospheric ozone during the austral spring has decreased sharply, mainly because of elevated concentrations of active chlorine [6]. Chlorofluorocarbons derived from anthropogenic emissions are converted into passive chlorine compounds (HCl and $ClONO_2$) that are then converted to active chlorine species by heterogeneous chemistry, which causes ozone depletion [7–9]. As the anthropogenic emissions of ozone-depleting

substances have been restricted since the Montreal Protocol, ozone concentrations in the Antarctic stratosphere are predicted to recover to pre-1980 values in 2060 [10–14].

Severe ozone depletion over the Arctic is relatively uncommon compared with that in the Antarctic. During normal Arctic winters, the polar vortex usually fractures and disperses early due to huge planetary wave activities and Brewer–Dobson circulation dynamics [15–17]. Thus, in the Arctic, the vortex duration is short, and the relative ozone loss is low [18]. However, irregular changes in Arctic ozone in recent years have attracted worldwide attention. The most severe Arctic ozone depletion lasted for nearly a month, from March to April 2020 [19]. Between mid-February and late March 2020, the persistence of unusually faint wave activities in the Arctic led to an abnormally persistent and cold vortex [20–22]. A prolonged cold vortex in the spring of 2020 accelerated the chemical depletion of ozone while hindering ozone transport from outside the vortex [23–25]. Bognar et al. found unprecedentedly low values of ozone VCD in the spring of 2020 using the ZSL-DOAS instrument over Eureka, Canada (80°N, 86°W) [26]. Bernhard et al. found a 25% increase in the average UV index at 10 Arctic and sub-Arctic regions during April 2020, compared with the historical average [5]. Furthermore, ozone chemical depletion in spring 2020 was well simulated by the Chemical Lagrangian Model of the Stratosphere and TOMCAT models [27–29]. This was the most severe low ozone event reported in the Arctic, worse than those in the springs of 1997 and 2011, and the powerful and persistent vortex is considered the main cause of significant ozone depletion in the region [30,31]. Arctic ozone loss events were reasonably predicted in the spring of 1997, 2011, and 2020, all of which were accompanied by extremely cold and strong polar vortices [32,33]. Moreover, the empirical relationship between the polar vortex strength and Arctic ozone can accurately predict Arctic ozone extremes.

Extremely low air temperatures are essential to produce polar stratospheric clouds (PSCs). PSCs provide a surface for the heterogeneous interactions that lead to the activation of halogens from halogen reservoirs, potentially causing serious reductions in ozone [34]. PSCs are classified into three types: nitric acid trihydrate (NAT), ice, and a supercooled ternary solution (STS), with threshold temperatures for existence at 195 K (T_{nat}), 188 K (T_{ice}), and 192 K (T_{sts}), respectively [9,35]. Although PSCs have multiple components [36,37], the temperature threshold for NAT provides a good estimate of the occurrence of heterogeneous chemistry [38,39]. PSCs might also grow large enough to precipitate and remove HNO_3 from the stratosphere, which is the reservoir of NO_2. The resulting denitrification from the polar vortex hinders chlorine deactivation by NO_2 [40,41]. For this to occur, the vortex must retain its low temperature and continue to act as a barrier to transport.

Analyses of the Arctic ozone depletion are invaluable for validating stratospheric ozone simulations and for understanding the underlying processes [27,42]. Currently, the ozone vertical column density (VCD), as detected by utilizing the characteristic ozone absorption in the UV and visible spectra, provides accurate, quantitative measurements of ozone. Ground-based observations of ozone VCD started in the first few decades of the twentieth century [43–45]. In the 1960s, ozonesondes were used to acquire atmospheric ozone data [46–48], and since 1978, satellite observations have provided essential data for atmospheric ozone-related studies [49]. Among these three methods, ground-based observations are crucial for calibrating remote sensing observations and optimizing retrieval results [50]. In the 1970s, differential optical absorption spectrometry (DOAS) was developed by Platt and Stutz [51] and has been widely used to measure several trace gases, including ozone, nitrogen dioxide, bromine monoxide, and sulfur dioxide [52]. In this study, we applied a ground-based DOAS system for ozone VCD observations in the Arctic [51]. The zenith scattered light observation mode was applied to measure ozone VCD using the Langley plot method [53]. This is meaningful to make accurate, long-term, ground-based observations in the polar regions.

We observed and validated the ozone depletion event (ODE) in the spring of 2020 above Ny-Ålesund, Norway. The methods and data are given in Section 2, which covers the presentation of the experimental location and DOAS instrument, the calculation of

ozone VCD, Global Ozone Monitoring Experiment 2 (GOME-2) observations, Brewer measurements, Système d'Analyze par Observation Zénithale (SAOZ) measurements, European Centre for Medium-Range Weather Forecast (ECMWF) data, and ozonesonde data. Section 3 presents the results; Section 3.1 describes ozone VCDs from February 2017 to October 2021 and the ozone difference in spring 2020. In Section 3.2, the daily variation in ozone VCDs obtained using zenith scattered light DOAS (ZSL-DOAS) was compared with the GOME-2 observations, Brewer, and SAOZ measurements. In Section 4.1, the ODE is illustrated using the sounding observations. The relationship between the Arctic ozone depletion and meteorological conditions in terms of temperature is described in Section 4.2, and a comprehensive summary is provided in Section 5.

2. Methods

2.1. Ozone VCD Observation

2.1.1. ZSL-DOAS Instrument and Experimental Location

We introduced a ZSL-DOAS instrument which included a prism, telescope, computer, filter, motor, and charge-coupled device (CCD) spectrometer. The motor controlled the telescope and could change the angle of elevation between the horizon and the zenith. The quartz fiber could transform the incident light; its numerical aperture was 0.22. The light is received by the spectrometer (Ocean Optics MAYA Pro) and measured using a 2048-pixel CCD. This spectrometer was designed for wavelengths between 290 and 429 nm and had a spectral resolution of 0.5 nm. The integration time varied between 100 and 2000 ms due to the light intensity. The detector operated normally at approximately 20 °C with a thermal controller. The mercury lamp spectra, offsets, and dark currents were calibrated ahead of the experiments. The instrument utilized the DOAS technique [51] to detect O_3, NO_2, $OClO$, BrO, and O_4. The DOAS principle is described in Appendix A.2. The ozone slant column density (SCD) was retrieved and raw data were obtained in the zenith direction (90°). The instrument was placed at the Yellow River Station (78.92°N, 11.93°E) in the Arctic. The DOAS instrument is highly accurate, can be left unattended, and can monitor multiple trace gases simultaneously. Compared with the Brewer and SAOZ especially, the instrument allows for better continuous monitoring. In the period from March to September 2020, in terms of the number of days that ozone was obtained over Ny-Ålesund, for example, there were 190 days of data from ZSL-DOAS, 123 days of data from Brewer, and 68 days of data from SAOZ. Figure 1 shows the ZSL-DOAS instrument and experimental location in Ny-Ålesund, Svalbard, Norway.
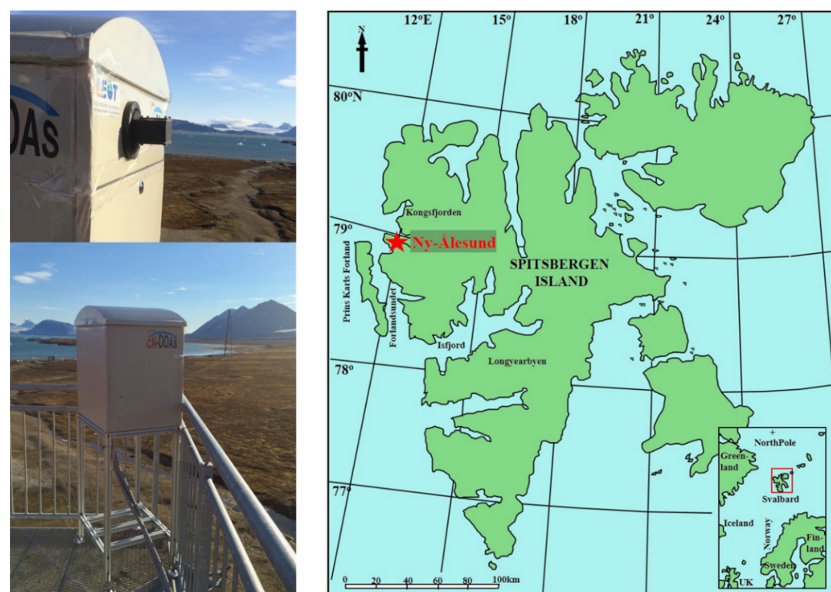

Figure 1. Ground-based ZSL-DOAS instrument and experimental site in Ny-Ålesund.

2.1.2. Calculation of Ozone VCD

We calculated the SCD for ozone using QDOAS [51]. QDOAS is a free software developed by the Royal Belgian Institute for Space Aeronomy (BIRA-IASB) (http://uv-vis.aeronomie.be/software/QDOAS/) that can retrieve trace gas concentrations. In the experiment, ozone was retrieved in the 320–340 nm band, and the gases involved in the retrieval included O_3 (223 K, 243 K), NO_2 (298 K), O_4 (293 K), and ring structures. Table 1 lists the parameters for the gases involved in the retrieval. Figure 2 shows a spectrum obtained during monitoring on 31 March 2020. The measured spectrum was fitted to give an ozone SCD of 1.06×10^{18} molec cm^{-2}, and the root mean square of spectral fitting residuals was 5.44×10^{-4}.

Table 1. Fitting parameters of spectral retrieval.

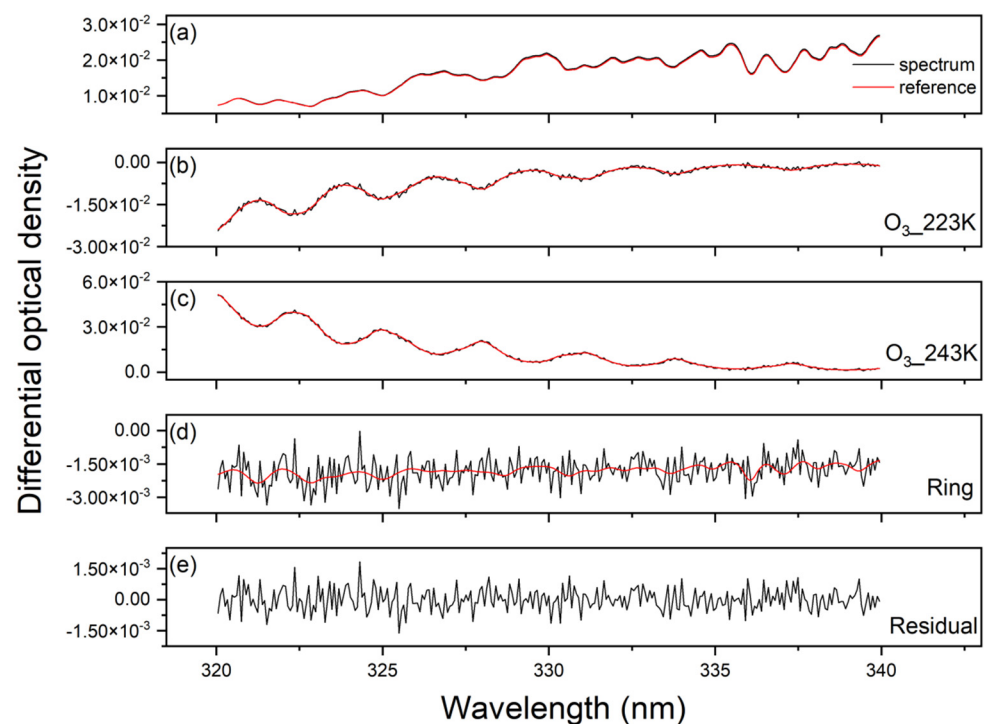| Parameters	References
O_3	223 K, 243 K [54]
O_4	293 K [55]
NO_2	298 K [56]
Ring	Calculated using QDOAS
Fitting Interval	320–340 nm
Polynomial	5

Figure 2. Spectrum fits of ozone on 31 March 2020.

The SCD is the column density on the diagonal path and the VCD is the column density on the vertical path. They are both in units of molecular cm^{-2}. As the SCD is dependent on the instrument's observation mode and the prevailing meteorological conditions, it is necessary to shift to the VCD, which is independent of the mode of observation:

$$AMF = \frac{SCD}{VCD} \tag{1}$$

Here, the air mass factor (AMF) can be obtained from the SCIATRAN model which is influenced by the a priori ozone profile, SZA (solar zenith angle), wavelength, and surface albedo. SCIATRAN is an atmospheric radiation transfer model containing retrieval

algorithms (http://www.iup.physik.uni-bremen.de/sciatran). The SCIATRAN model was developed by the Institute of Remote Sensing, University of Bremen, Germany. Based on the average monthly climate, the a priori ozone profile can be obtained. The SZA calculated in this study ranged between 35° and 80°, with surface albedos between 0.08 and 0.6. Table 2 lists these parameters. Since the "Ring effect" in the measurement caused by the Fraunhofer reference spectra can lead to lower trace gas levels in the retrieval than in the actual atmospheric levels, it is corrected with the following calculation:

$$dSCD(\alpha, \beta) = SCD(\alpha, \beta) - SCD_{FRS} = AMF(\alpha, \beta)VCD - SCD_{FRS} \qquad (2)$$

Table 2. Fitting parameter nodes for spectral retrieval.

Parameters	Nodes
SZA (°)	35, 40, 45, 50, 55, 60, 65, 70, 75, and 80
Surface albedo	0.05, 0.1, 0.2, 0.3, 0.4, 0.5, and 0.6
Wavelength (nm)	320 to 340 in intervals of 0.5

Here, SCD_{FRS} denotes the Fraunhofer absorption. In Formula (2), a linear fit is performed with AMF as the horizontal coordinate and dSCD as the vertical coordinate, where the absolute value of the intercept is the Fraunhofer absorption, and the slope is the VCD. Figure 3 presents the results of a linear fit of the dSCD and AMF on 31 March 2020. The correlation coefficient (R^2) was 0.99. The ozone VCD for this date was 6.53×10^{18} molec cm^{-2} and produced a fitting error of 2.76×10^{16} molec cm^{-2}.
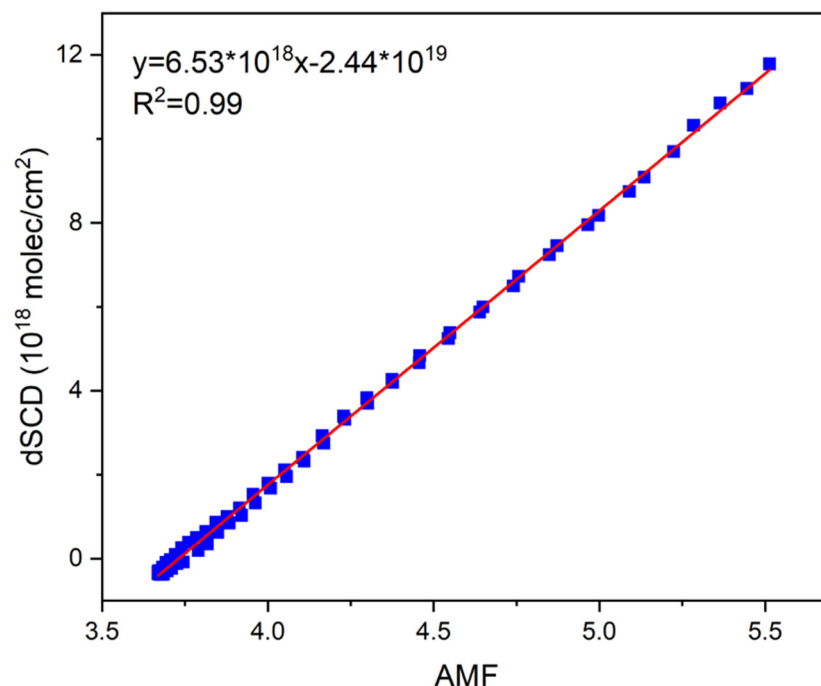

Figure 3. The linear fit between the ozone dSCDs and AMFs on 31 March 2020.

2.1.3. Error Estimation

Uncertainties in ozone VCD retrieval originate from uncertainties in the retrieval of the SCD and AMF. The error in retrieving the ozone SCD was 3.01%, within a 95% confidence interval. Table 2 provides the parameters used to calculate the AMF effect on wavelength. The uncertainties of the AMF due to wavelength selection were calculated as $(AMF_\lambda - AMF_{328})/AMF_\lambda$, where λ denotes the wavelength. Using the parameter nodes in Table 2, the uncertainties of the AMF in the wavelength were calculated to range from −4.257% to 4.630%, and the average uncertainty was 2.030%. Based on an evaluation of

the OMI ozone products, the AMF had an uncertainty of about 2% for the a priori ozone profile [57]. The average AMF uncertainty was calculated as 2.85% using the following equation: $\sqrt{AMF_{wave}^2 + AMF_{profile}^2}$, where AMF_{wave} denotes the error of AMF influenced by wavelength, and $AMF_{profile}$ denotes the AMF error affected through the a priori ozone profile. The total error in the retrieved ozone VCD was 4.15%, calculated using the following error equation: $E_{VCD} = \sqrt{E_{SCD}^2 + E_{AMF}^2}$, where E_{SCD} and E_{AMF} denote the errors of the SCD and AMF, respectively.

2.2. Auxiliary Data

GOME-2 has a band between 240 and 790 nm, a spectral resolution ranging from 0.2 to 0.5 nm, and a nominal swath width spatial resolution of 80×40 km^2 [58]. The GOME-2 dataset included the daily mean VCD data (source: https://avdc.gsfc.nasa.gov/, accessed on 18 June 2022). Brewer spectrophotometers used holographic diffraction gratings to obtain the directly transmitted intensity of sunlight [59]. Ozone columns were calculated by averaging five consecutive measurements. The daily mean ozone data were obtained from the Brewer dataset (source: https://woudc.org/, accessed on 18 June 2022). The SAOZ instrument was a UV-Vis spectrometer belonging to a global network of analogous instruments [60]. The SAOZ instrument provided a viewing angle of approximately 20° and measured trace gas concentrations in the stratosphere based on DOAS technology [51]. Hendrick et al. calculated an error of 5.9% for the measurement of ozone by SAOZ [61]. The SAOZ dataset was used to obtain the daily mean ozone VCD data (source: http://saoz.obs.uvsq.fr/, accessed on 18 June 2022).

The ERA5 hourly pressure-level data from 1959 to 2022 used for daily temperatures in this study was obtained from the ECMWF website (source: https://www.ecmwf.int/en/newsletter/147/news/era5-reanalysis-production, accessed on 18 June 2022). Since 1992, the Alfred Wegener Institute has recorded the total ozone column and vertical profile using a balloon-borne ozonesonde in Ny-Ålesund. In 2020, the temporal resolution of the sounding data from 25 March to 13 April was once per day, compared with once per 3 d during the spring and once per week during the other seasons (source: https://ndacc.larc.nasa.gov/, accessed on 17 April 2023).

3. Results

3.1. Ozone VCDs

The ozone VCDs obtained from the GOME-2 satellite, Brewer, SAOZ, and ground-based instrument from February 2017 to October 2021 over Ny-Ålesund are shown in Figure 4. In 2017, 2018, 2019, and 2021, the ozone VCD showed a fluctuating downward trend between March and September, with small increases around March and August. In 2020, however, severe ozone depletion occurred between 18 March and 18 April, after which the ozone VCD increased gradually. The ozone VCD decreased further in mid-May and around September, the ozone VCD increased again, probably due to the clear warming of the polar stratosphere.

The ozone data for 2020 and average ozone data for the other years from the ZSL-DOAS instrument, as well as satellite observations from GOME-2 and measurements from the Brewer and SAOZ instruments over Ny-Ålesund, are shown in Figure 5. The average ozone VCD from ZSL-DOAS between 18 March and 18 April 2020 was abnormally low at ~274.8 DU, only 64.7 ± 0.1% of what was observed in the other four years. In addition, the daily peak difference was 195.7 DU during this period. The minimum ozone VCD from ZSL-DOAS was 241.2 DU on 5 April. We also analyzed the diurnal means of the relative ozone difference between the 2020 data and the mean of the other four years. Compared to the other four years, the 2020 daily average relative differences from 18 March to 18 April from the GOME-2, ZSL-DOAS, Brewer, and SAOZ datasets were −36.5%, −35.3 ± 0.4%, −33.1 ± 0.7%, and −32.0 ± 0.1%, respectively. All instruments detected relatively low levels of ozone from 18 March to 18 April 2020.
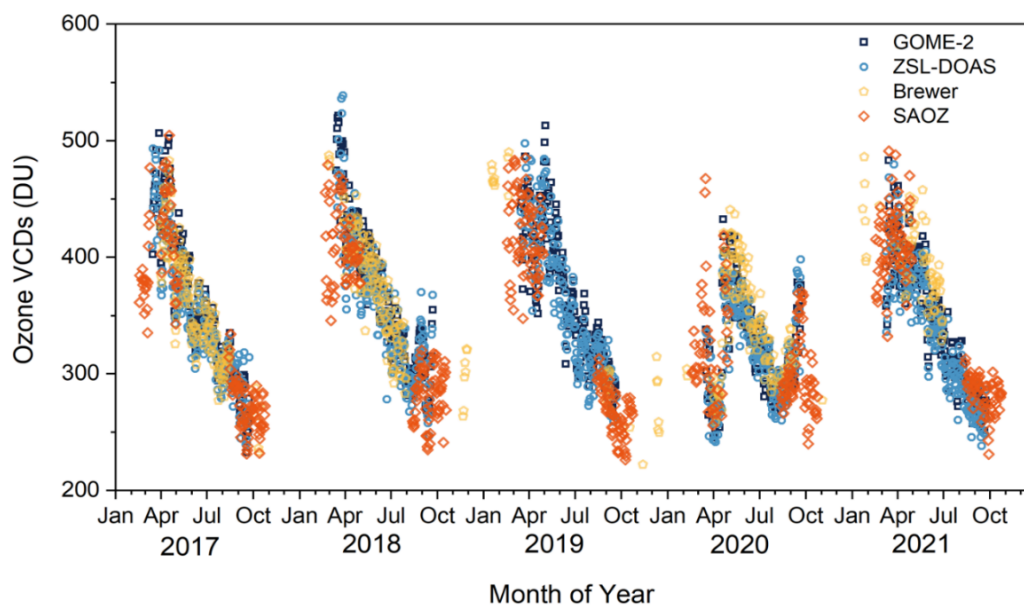
Figure 4. Ozone VCDs over Ny-Ålesund from ZSL-DOAS, GOME-2, Brewer, and SAOZ.
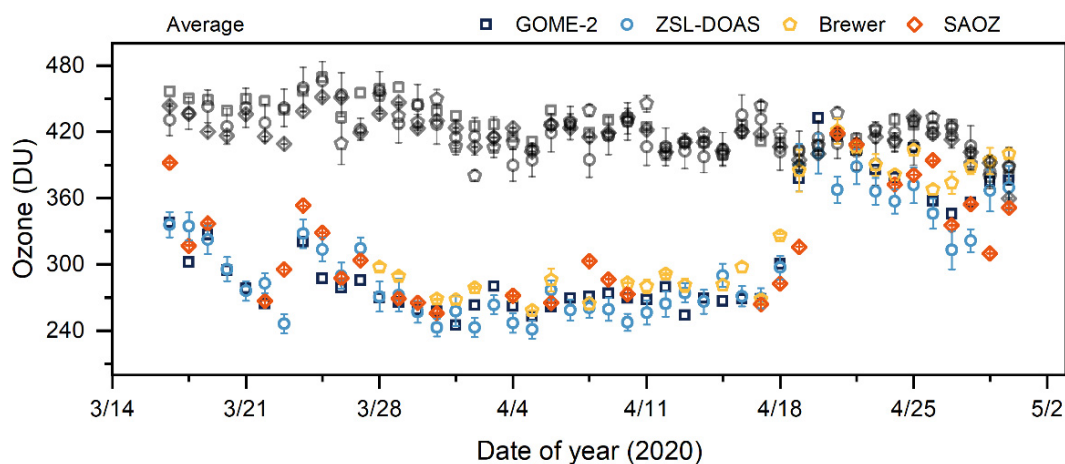

Figure 5. Ozone data over Ny-Ålesund for 2020 and the average ozone data (black) for 2017, 2018, 2019, and 2021.

3.2. Descriptive Statistical Analysis

Ozone VCDs from the ZSL-DOAS, GOME-2, Brewer, and SAOZ datasets were analyzed based on the empirical cumulative density function (ECDF), boxplots, Pearson's correlation coefficients, and relative deviations. The ECDF was used to characterize the distribution of the data, wherein the horizontal coordinates of the ECDF plot were the ozone VCDs and the vertical coordinates were the cumulative probabilities. When the ZSL-DOAS dataset was compared to the other datasets, we performed analyses only for the number of days for which both datasets had values, thereby enabling us to compare and analyze their ozone VCDs.

As can be seen in Figure 6a–c, the values of ozone VCDs from the ZSL-DOAS dataset were strongly correlated with the data from GOME-2 and SAOZ at lower and higher values. Of the ozone VCDs from the ZSL-DOAS data, 1–60% were distributed in the 230–350 DU range. Between 350 and 400 DU, the ozone VCDs of GOME-2 were clearly higher than those of ZSL-DOAS. A comparison between the ZSL-DOAS and Brewer data revealed that there is good consistency between the two instruments. Results of the ozone VCDs from Brewer were slightly overestimated, which can be attributed to the fact that the final calibration of the Brewer instrument at Ny-Ålesund was in 2018, a conclusion that was also arrived

at in a previous study [62]. However, in the range from 280 to 350 DU, the ozone VCDs from SAOZ were lower than those from ZSL-DOAS, whereas between 370 and 410 DU, the SAOZ ozone VCDs were overestimated. As visualized using boxplots, compared with ozone VCDs from GOME-2, the ozone VCDs from ZSL-DOAS were characterized by high outliers and lower mean values, with more concentrated values and less volatility. These latter ozone VCDs also included higher outliers compared with those for VCDs based on a Brewer analysis and had smaller overall values and less data volatility. Unlike the values obtained based on the GOME-2 and Brewer data, the mean ozone VCDs from SAOZ were lower than those of ZSL-DOAS, and the distribution interval of these values was smaller than that of the ZSL-DOAS. Differences between these ozone data may be related to retrieval settings (choices of fitting the interval and absorption cross-sections) and the temperature dependence of the different instruments [61,63]. Furthermore, there might be a mismatch of measurement positions between the ZSL-DOAS and the GOME-2 instruments [64,65].
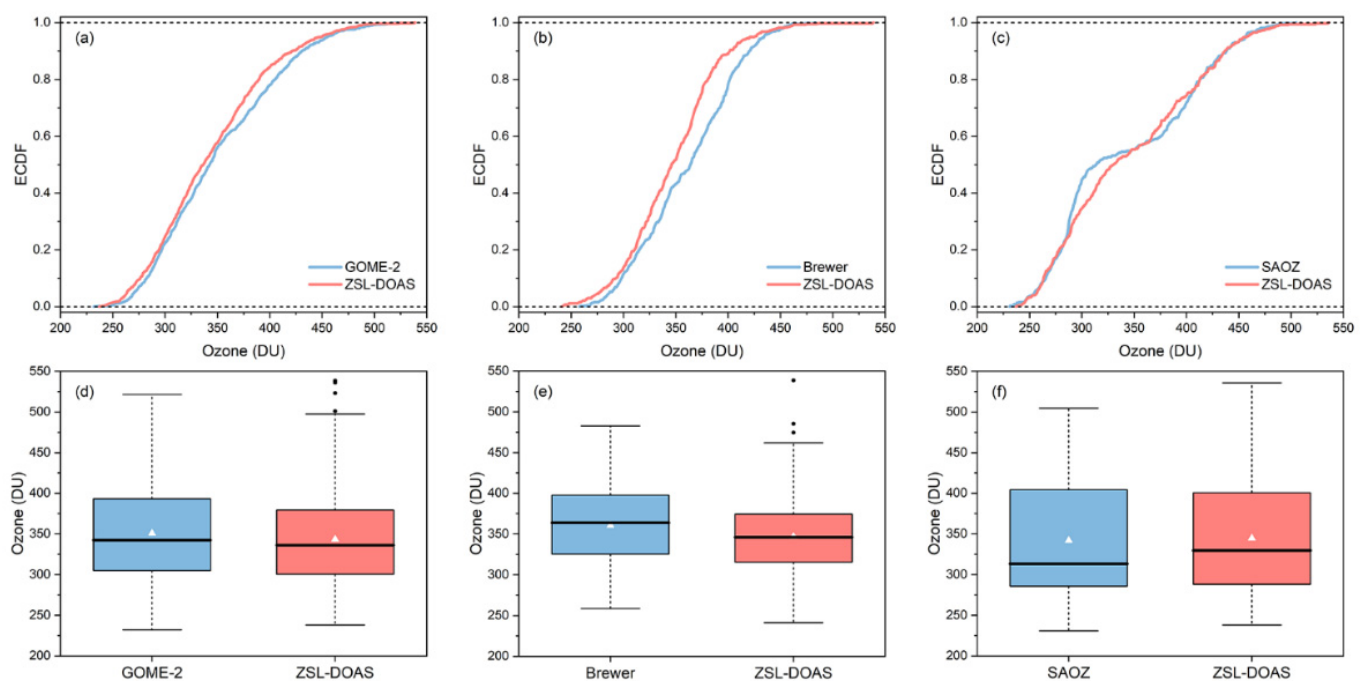

Figure 6. ECDF plots of ozone VCDs from ZSL-DOAS with (**a**) GOME-2, (**b**) Brewer, and (**c**) SAOZ. Boxplots of ozone VCDs from ZSL-DOAS with (**d**) GOME-2, (**e**) Brewer, and (**f**) SAOZ. In the boxplots, the black central bar indicates the median and the white triangle indicates the mean value.

Figure 7 presents the linear fit between the observed ozone VCDs and GOME-2 observations, Brewer, and SAOZ measurements. The Pearson correlation coefficients were relatively high at 0.97, 0.87, and 0.91, respectively. In addition, the relative deviations were 2.3%, 3.1%, and 3.5%, respectively. The ground-based DOAS measurements were highly correlated with the ozone VCDs observed using GOME-2 onboard the MetOp satellite and with those obtained using the Brewer and SAOZ instruments. The ZSL-DOAS ozone VCDs were consistent with the GOME-2, Brewer, and SAOZ observations over Ny-Ålesund. Thus, the observation of the VCDs of the Arctic ozone using a ground-based DOAS instrument was reliable and valid.
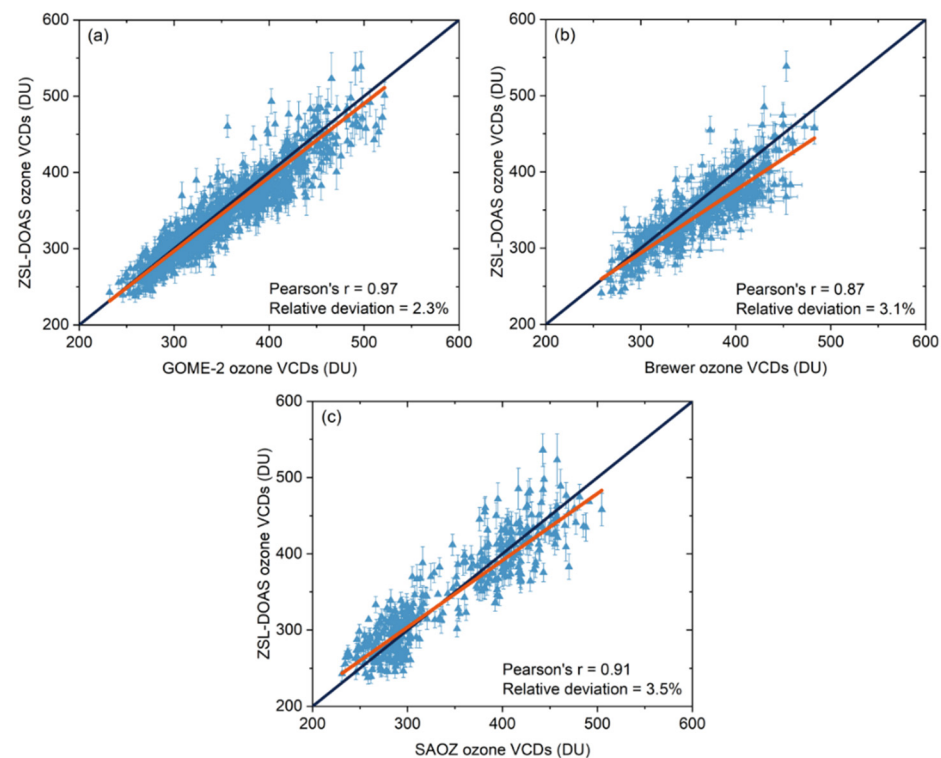
Figure 7. Scatter plots and linear fits of the retrieved ozone VCDs with (**a**) GOME-2, (**b**) Brewer, and (**c**) SAOZ.

4. Discussion

4.1. Arctic Ozone Depletion Based on Ozonesonde Data

Figure 8a–j presents the ozone and temperature profiles from the ozonesonde data above Ny-Ålesund between 2017 and 2021 from January to July of each year. In 2017, no sounding data were obtained prior to March 22. The ozone profile (Figure A1b) above Ny-Ålesund from 9 January to 1 July of 2020 from the ERA5 data and the relative differences (Figure A1c) between ozonesonde and ERA5 are shown in Appendix A.1. We analyzed the relative differences between the ozonesonde and ERA5 data and the average absolute relative difference between ozonesonde and ERA5 was 0.31 ppmv. The ERA5 data were consistent with the ozonesonde data. Over Ny-Ålesund, ozone is mainly present above an altitude of 16 km, and the mixing ratio of ozone occurring below 16 km is less than 2.5 ppmv. Comparatively, during the period spanning January–February in 2018, the mixing ratios of ozone present in the lower stratospheric region above 16 km were mostly less than 3.5 ppmv, which is significantly lower than the values obtained in 2019 and 2021. From January to February 2018, the lower stratospheric region over Ny-Ålesund was characterized by colder temperature conditions than those recorded in 2019 and 2021. Indeed, the temperature in the 16–25 km altitude range was lower than T_{nat}, thereby providing conditions favorable for PSC formation. PSCs provide a surface for heterogeneous interactions, leading to halogen activation and severe ozone depletion. However, in 2020, the temperature conditions were cold, and the cold temperatures lasted longer than the corresponding duration in 2018; it was not until mid-April that temperatures began to climb significantly. In January and March 2020, the temperatures in the 15–25 km altitude range were lower than T_{nat}, also providing conditions conducive to PSC formation. In January and early February of 2020, the mixing ratios of ozone present in the 16–20 km altitude range were below 3.0 ppmv, as were the mixing ratios during early February and early March of that year, whereas, in mid-March and mid-April of 2020, the ozone mixing ratios in the 16–20 km altitude range were below 1.0 ppmv and even partly below 0.5 ppmv. Even in 2011, when severe ozone depletion occurred, the ozone mixing ratio was above 0.5 ppmv over the Arctic [66].
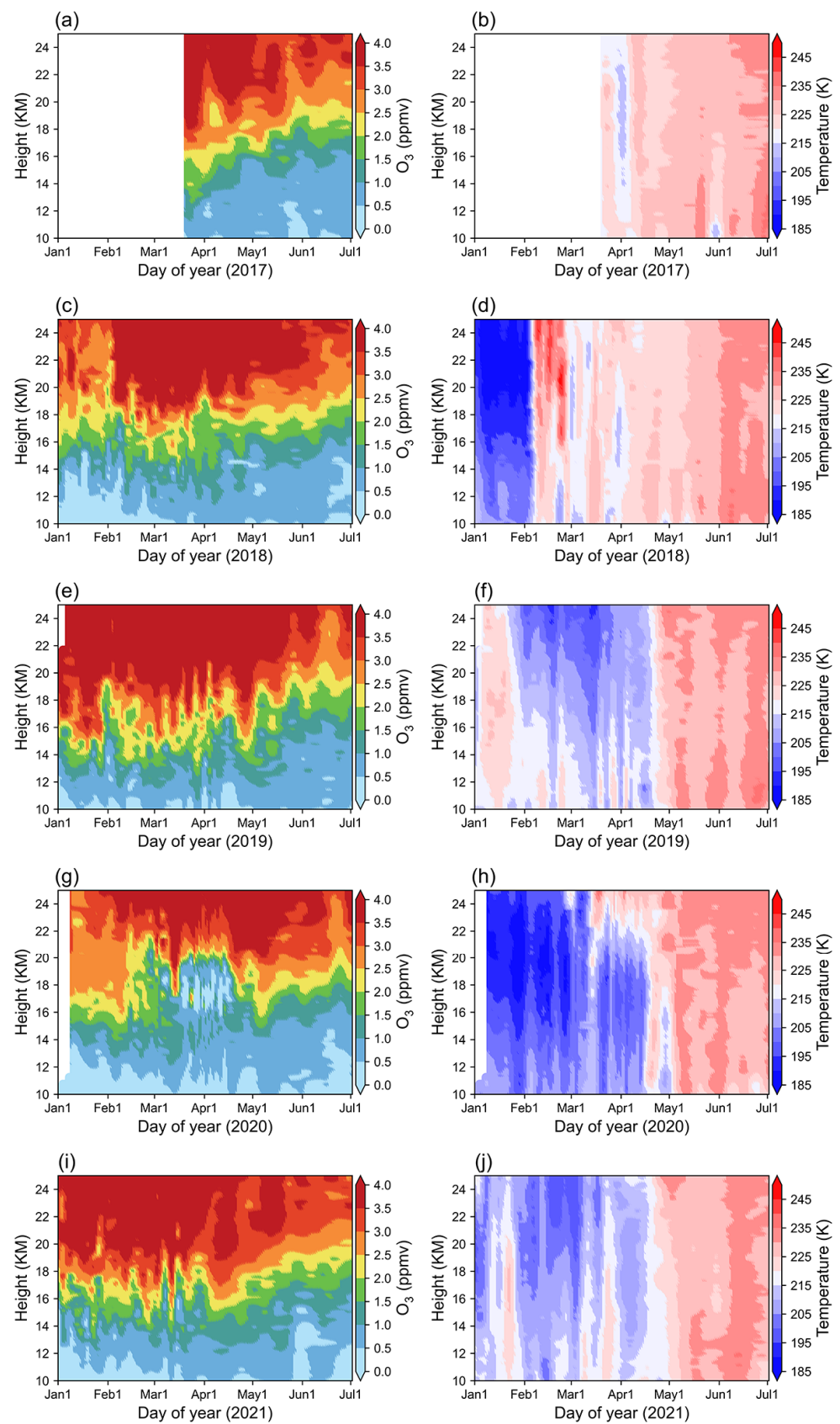
Figure 8. The ozone profiles, above Ny-Ålesund, from January to July of each year for (**a**) 2017, (**c**) 2018, (**e**) 2019, (**g**) 2020, and (**i**) 2021, and the temperature profiles for (**b**) 2017, (**d**) 2018, (**f**) 2019, (**h**) 2020, and (**j**) 2021.

The sounding observations similarly provided evidence to indicate the occurrence of Arctic stratospheric ozone depletion during the spring of 2020. Furthermore, severe ozone depletion occurred between mid-March and mid-April 2020 in the 16–20 km altitude range over Ny-Ålesund, which was strongly associated with persistently low-temperature conditions during the spring of that year.

4.2. Associations between Arctic Ozone Depletion and Meteorological Conditions

To further study the associations between Arctic ozone depletion and temperature conditions, we used the ERA5 data. The daily average temperatures in Ny-Ålesund between November 2016 and September 2021 were obtained at 70 hPa (–17.5 km) in the low stratosphere, where significant ozone depletion tends to occur (Figure 9). Furthermore, temperatures dropped below the threshold (195 K) at which PSCs exist. A relatively colder stratosphere over Ny-Ålesund persisted for a longer duration during the winter of 2019/2020 than in previous years, with air temperatures as low as 190 K. The number of days with daily temperatures below 195 K during the winters of 2017/2018, 2019/2020, and 2020/2021 are shown in Table 3. In addition, the overall winter temperatures in 2019/2020 were lower than those of the same period in the other years and included a prolonged period of cold temperatures, leading to prolonged PSCs. As a result of the atypically faint wave activities that occurred between mid-February and late March 2020 over the Northern Hemisphere [19], the abrupt warming in spring 2020 was weaker than warming in the other four years. The 2019/2020 winter was the coldest recorded in the Arctic in the past 40 years [21,24].
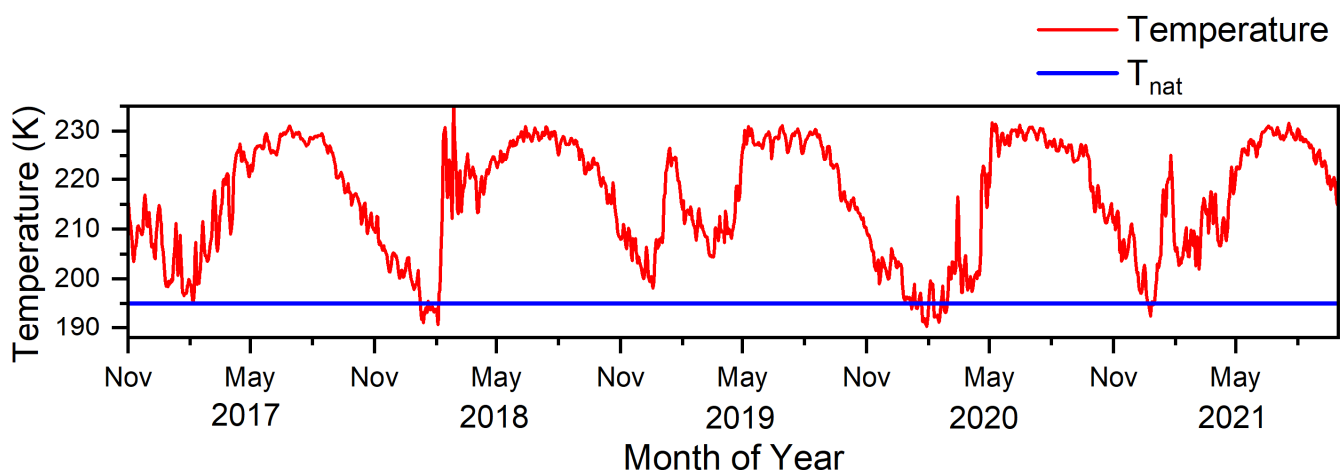

Figure 9. Temperatures (at 70 hPa) over Ny-Ålesund from November 2016 to September 2021; the blue line denotes the threshold temperature for the formation of PSCs.

Table 3. Days below T_{nat} and daily average temperatures (December–February).

Date	Days below T_{nat}	Temperature (K) (Average/Range)
2016.12–2017.2	0	203.5/195.2–214.8
2017.12–2018.2	26	203.6/190.6–236.2
2018.12–2019.2	0	211.8/198.1–226.5
2019.12–2020.2	32	196.9/190.2–206.1
2020.12–2021.2	6	205.3/192.5–225.1

A cold and stable polar vortex is a prerequisite for ensuring that Arctic stratospheric temperatures are sufficiently low. The 2019/2020 winter was unique, and the polar vortex was unusually stable, prolonged, and cold [24,32]. A large and strong Arctic vortex lasted from early December into the final week of April, which is almost unheard of [21,67]. The faint planetary wave activity in the Northern Hemisphere also contributed to the formation of a cold and strong vortex [28]. Unusually low temperatures and a strong and prolonged

vortex in the 2019/2020 winter provided favorable meteorological conditions for ozone depletion in the Arctic.

5. Conclusions

In this research, we measured the ozone VCD using the ZSL-DOAS instrument for 5 years and compared the results with those obtained with the GOME-2 satellite and the Brewer and SAOZ instruments. Compared to the other four years, the 2020 daily average relative differences from March 18 to April 18 from the GOME-2, ZSL-DOAS, Brewer, and SAOZ datasets were -36.5%, $-35.3 \pm 0.4\%$, $-33.1 \pm 0.7\%$, and $-32.0 \pm 0.1\%$, respectively. All instruments recorded severe ozone depletion from March 18 to April 18, 2020.

In addition, the ozone VCDs from the ZSL-DOAS, GOME-2, Brewer, and SAOZ datasets were analyzed in a statistical framework based on the ECDF, boxplots, Pearson's correlation coefficients, and relative deviations. The ECDF results indicated that the ozone VCDs from the ZSL-DOAS dataset are strongly correlated with the data from GOME-2 and SAOZ at lower and higher values and the ozone VCDs from Brewer are overestimated. Compared with the GOME-2 and Brewer data, the ozone VCDs from ZSL-DOAS were smaller and there was less data volatility. However, the mean values of the ozone VCDs from ZSL-DOAS were higher than those of SAOZ, and the distribution interval of these values was larger than that of the SAOZ. We further evaluated a correlation analysis with the GOME-2 satellite and the Brewer and SAOZ instruments, revealing Pearson correlation coefficients of 0.97, 0.87, and 0.91, respectively. In addition, the relative deviations were 2.3%, 3.1%, and 3.5%, respectively. The ZSL-DOAS ozone VCDs were consistent with the GOME-2, Brewer, and SAOZ observations over Ny-Ålesund. Therefore, we can conclude that the method of observing the VCDs of the Arctic ozone using a ground-based DOAS instrument was reliable and valid.

The sounding and ERA5 data indicated severe ozone depletion between mid-March and mid-April 2020 in the 16–20 km altitude range over Ny-Ålesund, which was strongly associated with the persistently low temperatures in the spring of 2020. The overall winter temperatures in 2019/2020 were lower than those of the same period in the other years and included a prolonged period with cold temperatures. Furthermore, the unusually low temperatures and a strong and prolonged vortex in the 2019/2020 winter provided favorable meteorological conditions for ozone depletion in the Arctic.

In summary, using ZSL-DOAS observations, we provided evidence for the unprecedented ozone depletion during the Arctic spring of 2020. The ZSL-DOAS ozone VCD observations are consistent with the GOME-2 observations, Brewer, and SAOZ measurements, and provide support for continuous ozone columns above the polar area. This is essential for the study of polar ozone changes and its effect on climate change and ecological conditions.

Appendix A

Appendix A.1. Ozone Profiles from Ozonesonde and ERA5
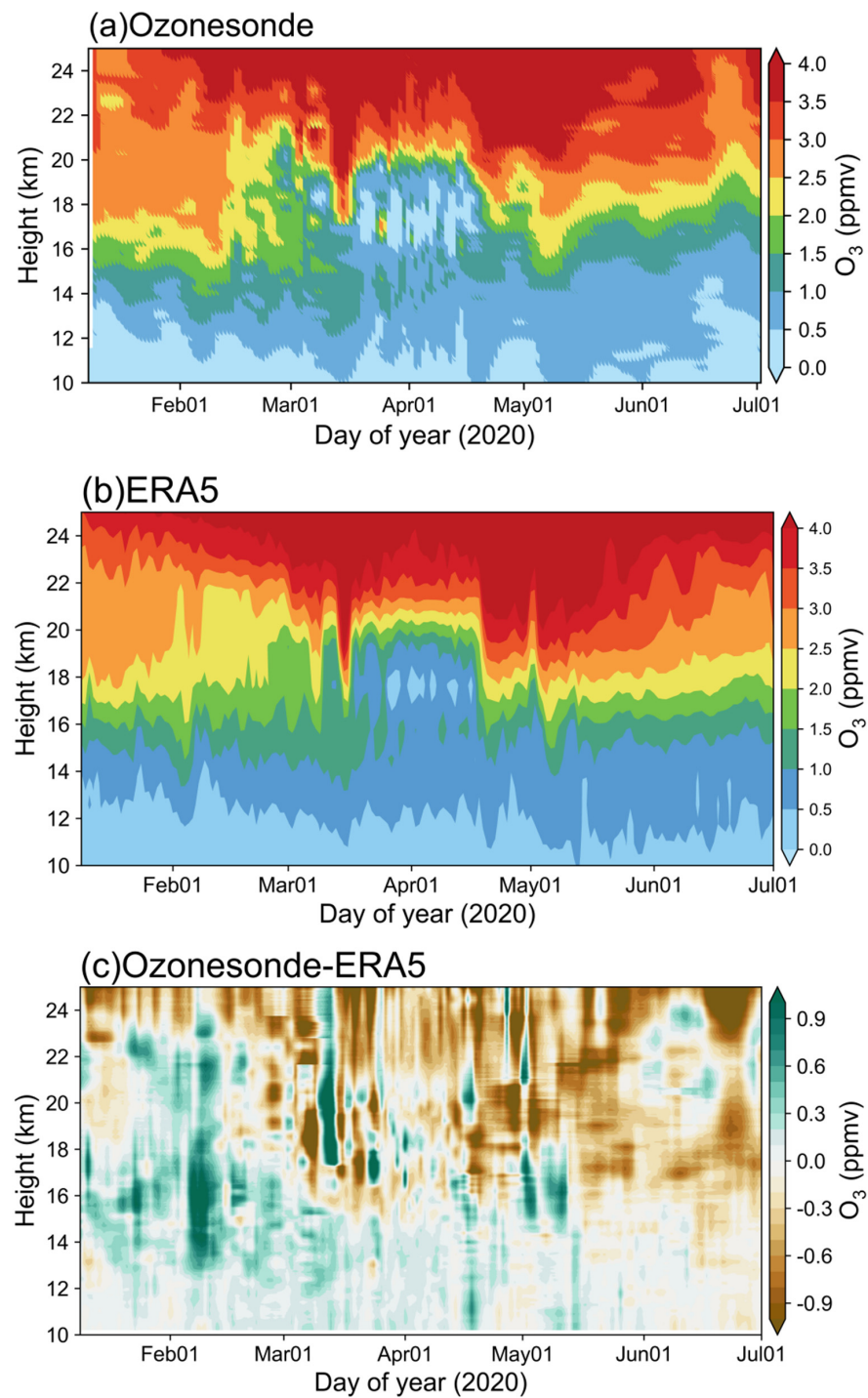

Figure A1. The ozone profiles, above Ny-Ålesund, from 9 January to 1 July 2020 from (**a**) ozonesonde and (**b**) ERA5, and (**c**) the relative differences between ozonesonde and ERA5.

Appendix A.2. Principle of DOAS

Based on the different absorption bands and characteristic peaks of various gases and their measured intensity, we can retrieve the content of each trace gas according to the Lambert–Beer law as follows:

$$I(\lambda) = I_0(\lambda) * exp\left\{-\int_0^L \left[\sum_{j=1}^n \sigma_j(\lambda) * c_j(s) + \varepsilon_M(\lambda) + \varepsilon_R(\lambda)\right] ds\right\} * A(\lambda) \tag{A1}$$

Here, $I_0(\lambda)$ represents the original light intensity of the luminophore at the wavelength λ, $I(\lambda)$ denotes the light intensity received by the detector at the wavelength λ, L represents the distance traveled by the incident light in the absorbing gas, $\sigma_j(\lambda)$ represents the absorption cross-section for the jth gas, $c_j(s)$ denotes the concentration of the jth gas at the s position, n is the number of types of gas measured, $\varepsilon_M(\lambda)$ and $\varepsilon_R(\lambda)$ are the extinction coefficients for Mie scattering and Rayleigh scattering, respectively, and $A(\lambda)$ represents instrumental effects and turbulence [51].

The spectral absorption structures $\sigma_j(\lambda)$ include the broadband $\sigma_{j0}(\lambda)$ and narrowband $\sigma_j'(\lambda)$ absorption structures. Thus, Formula (A1) can be written as:

$$\begin{aligned} I(\lambda) = I_0(\lambda) * exp\left\{-\int_0^L \left[\sum_{j=1}^n \sigma_j'(\lambda) * c_j(s)\right] ds\right\} \\ *exp\left\{-\int_0^L \left[\sum_{j=1}^n \sigma_{j0}(\lambda) * c_j(s) + \varepsilon_M(\lambda) + \varepsilon_R(\lambda)\right] ds\right\} * A(\lambda) \end{aligned} \tag{A2}$$

$I_0'(\lambda)$ denotes the intensity in the absence of differential absorption:

$$I_0'(\lambda) = I_0(\lambda) * exp\left\{-\int_0^L \left[\sum_{j=1}^n \sigma_{j0}(\lambda) * c_j(s) + \varepsilon_M(\lambda) + \varepsilon_R(\lambda)\right] ds\right\} * A(\lambda) \tag{A3}$$

$SCD_j = \int_0^L c_j(s) ds$ represents the SCD of the jth gas. Then, we obtain the differential optical density D':

$$D' = \ln\frac{I_0'(\lambda)}{I(\lambda)} = \int_0^L \left[\sum_{j=1}^n \sigma_j'(\lambda) * c_j(s)\right] ds = \sum_{j=1}^n \sigma_j'(\lambda) * SCD_j \tag{A4}$$

References

1. Solomon, S.; Garcia, R.R.; Rowland, F.S.; Wuebbles, D.J. On the depletion of Antarctic ozone. *Nature* **1986**, *321*, 755–758. [CrossRef]
2. Chipperfield, M.P.; Bekki, S.; Dhomse, S.; Harris, N.R.P.; Hassler, B.; Hossaini, R.; Steinbrecht, W.; Thiéblemont, R.; Weber, M. Detecting recovery of the stratospheric ozone layer. *Nature* **2017**, *549*, 211–218. [PubMed]
3. McKenzie, R.L.; Aucamp, P.J.; Bais, A.F.; Bjorn, L.O.; Ilyas, M.; Madronich, S. Ozone depletion and climate change: Impacts on UV radiation. *Photochem. Photobiol. Sci.* **2011**, *10*, 182–198.
4. Bernhard, G.; Dahlback, A.; Fioletov, V.; Heikkilä, A.; Johnsen, B.; Koskela, T.; Lakkala, K.; Svendby, T. High levels of ultraviolet radiation observed by ground-based instruments below the 2011 Arctic ozone hole. *Atmos. Chem. Phys.* **2013**, *13*, 10573–10590.
5. Bernhard, G.H.; Fioletov, V.E.; Grooss, J.U.; Ialongo, I.; Johnsen, B.; Lakkala, K.; Manney, G.L.; Muller, R.; Svendby, T. Record-Breaking Increases in Arctic Solar Ultraviolet Radiation Caused by Exceptionally Large Ozone Depletion in 2020. *Geophys. Res. Lett.* **2020**, *47*, e2020GL090844. [CrossRef] [PubMed]
6. Farman, J.C.; Gardiner, B.G.; Shanklin, J.D. Large losses of total ozone in Antarctica reveal seasonal ClO_x/NO_x interaction. *Nature* **1985**, *315*, 207–210. [CrossRef]
7. Solomon, S. Stratospheric ozone depletion: A review of concepts and history. *Rev. Geophys.* **1999**, *37*, 275–316.
8. Müller, R.; Grooß, J.-U.; Zafar, A.M.; Robrecht, S.; Lehmann, R. The maintenance of elevated active chlorine levels in the Antarctic lower stratosphere through HCl null cycles. *Atmos. Chem. Phys.* **2018**, *18*, 2985–2997. [CrossRef]
9. Tritscher, I.; Pitts, M.C.; Poole, L.R.; Alexander, S.P.; Cairo, F.; Chipperfield, M.P.; Grooß, J.U.; Höpfner, M.; Lambert, A.; Luo, B. Polar stratospheric clouds: Satellite observations, processes, and role in ozone depletion. *Rev. Geophys.* **2021**, *59*, e2020RG000702. [CrossRef]
10. Solomon, S.; Ivy, D.J.; Kinnison, D.; Mills, M.J.; Neely, R.R.; Schmidt, A. Emergence of healing in the Antarctic ozone layer. *Science* **2016**, *353*, 269–274. [CrossRef]
11. Kuttippurath, J.; Nair, P.J. The signs of Antarctic ozone hole recovery. *Sci. Rep.* **2017**, *7*, 585.

12. Strahan, S.E.; Douglass, A.R. Decline in Antarctic Ozone Depletion and Lower Stratospheric Chlorine Determined from Aura Microwave Limb Sounder Observations. *Geophys. Res. Lett.* **2018**, *45*, 382–390. [CrossRef]

13. WMO. Scientific Assessment of Ozone Depletion: 2022. In *World Meteorological Organization Ozone Research and Monitorin*; WMO: Geneva, Switzerland, 2022; GAW Report No. 278; p. 509.

14. Stone, K.A.; Solomon, S.; Kinnison, D.E.; Mills, M.J. On Recent Large Antarctic Ozone Holes and Ozone Recovery Metrics. *Geophys. Res. Lett.* **2021**, *48*, e2021GL095232. [CrossRef] [PubMed]

15. Manney, G.L.; Froidevaux, L.; Santee, M.L.; Livesey, N.J.; Sabutis, J.L.; Waters, J.W. Variability of ozone loss during Arctic winter (1991–2000) estimated from UARS Microwave Limb Sounder measurements. *J. Geophys. Res. Atmos.* **2003**, *108*, 4149. [CrossRef]

16. Dameris, M. Climate change and atmospheric chemistry: How will the stratospheric ozone layer develop? *Angew. Chem. Int. Ed.* **2010**, *49*, 8092–8102. [CrossRef] [PubMed]

17. Harris, N.; Lehmann, R.; Rex, M.; von der Gathen, P. A closer look at Arctic ozone loss and polar stratospheric clouds. *Atmos. Chem. Phys.* **2010**, *10*, 8499–8510.

18. Solomon, S.; Portmann, R.W.; Thompson, D.W. Contrasts between Antarctic and Arctic ozone depletion. *Proc. Natl. Acad. Sci. USA* **2007**, *104*, 445–449. [CrossRef]

19. Dameris, M.; Loyola, D.G.; Nützel, M.; Coldewey-Egbers, M.; Lerot, C.; Romahn, F.; Van Roozendael, M. Record low ozone values over the Arctic in boreal spring 2020. *Atmos. Chem. Phys.* **2021**, *21*, 617–633.

20. Hu, Y. The very unusual polar stratosphere in 2019–2020. *Sci. Bull.* **2020**, *65*, 1775–1777. [CrossRef]

21. Kuttippurath, J.; Feng, W.; Müller, R.; Kumar, P.; Raj, S.; Gopikrishnan, G.P.; Roy, R. Exceptional loss in ozone in the Arctic winter/spring of 2019/2020. *Atmos. Chem. Phys.* **2021**, *21*, 14019–14037.

22. Ardra, D.; Kuttippurath, J.; Roy, R.; Kumar, P.; Raj, S.; Müller, R.; Feng, W. The unprecedented ozone loss in the Arctic winter and spring of 2010/2011 and 2019/2020. *ACS Earth Space Chem.* **2022**, *6*, 683–693. [CrossRef]

23. Manney, G.L.; Livesey, N.J.; Santee, M.L.; Froidevaux, L.; Lambert, A.; Lawrence, Z.D.; Millán, L.F.; Neu, J.L.; Read, W.G.; Schwartz, M.J. Record-low Arctic stratospheric ozone in 2020: MLS observations of chemical processes and comparisons with previous extreme winters. *Geophys. Res. Lett.* **2020**, *47*, e2020GL089063. [CrossRef]

24. Lawrence, Z.D.; Perlwitz, J.; Butler, A.H.; Manney, G.L.; Newman, P.A.; Lee, S.H.; Nash, E.R. The remarkably strong Arctic stratospheric polar vortex of winter 2020: Links to record-breaking Arctic oscillation and ozone loss. *J. Geophys. Res. Atmos.* **2020**, *125*, e2020JD033271.

25. Inness, A.; Chabrillat, S.; Flemming, J.; Huijnen, V.; Langenrock, B.; Nicolas, J.; Polichtchouk, I.; Razinger, M. Exceptionally low Arctic stratospheric ozone in spring 2020 as seen in the CAMS reanalysis. *J. Geophys. Res. Atmos.* **2020**, *125*, e2020JD033563. [CrossRef]

26. Bognar, K.; Alwarda, R.; Strong, K.; Chipperfield, M.P.; Dhomse, S.S.; Drummond, J.R.; Feng, W.; Fioletov, V.; Goutail, F.; Herrera, B. Unprecedented spring 2020 ozone depletion in the context of 20 years of measurements at Eureka, Canada. *J. Geophys. Res. Atmos.* **2021**, *126*, e2020JD034365. [CrossRef]

27. Grooß, J.-U.; Müller, R. Simulation of record Arctic stratospheric ozone depletion in 2020. *J. Geophys. Res. Atmos.* **2021**, *126*, e2020JD033339. [CrossRef]

28. Feng, W.; Dhomse, S.S.; Arosio, C.; Weber, M.; Burrows, J.P.; Santee, M.L.; Chipperfield, M.P. Arctic ozone depletion in 2019/20: Roles of chemistry, dynamics and the Montreal Protocol. *Geophys. Res. Lett.* **2021**, *48*, e2020GL091911. [CrossRef]

29. Weber, M.; Arosio, C.; Feng, W.; Dhomse, S.S.; Chipperfield, M.P.; Meier, A.; Burrows, J.P.; Eichmann, K.-U.; Richter, A.; Rozanov, A. The unusual stratospheric Arctic winter 2019/20: Chemical ozone loss from satellite observations and TOMCAT chemical transport model. *J. Geophys. Res. Atmos.* **2021**, *126*, e2020JD034386. [CrossRef]

30. Hansen, G.; Chipperfield, M.P. Ozone depletion at the edge of the Arctic polar vortex 1996/1997. *J. Geophys. Res. Atmos.* **1999**, *104*, 1837–1845. [CrossRef]

31. Manney, G.L.; Santee, M.L.; Rex, M.; Livesey, N.J.; Pitts, M.C.; Veefkind, P.; Nash, E.R.; Wohltmann, I.; Lehmann, R.; Froidevaux, L.; et al. Unprecedented Arctic ozone loss in 2011. *Nature* **2011**, *478*, 469–475.

32. Rao, J.; Garfinkel, C.I. Arctic Ozone Loss in March 2020 and its Seasonal Prediction in CFSv2: A Comparative Study With the 1997 and 2011 Cases. *J. Geophys. Res. Atmos.* **2020**, *125*, e2020JD033524. [CrossRef]

33. Rao, J.; Garfinkel, C.I. The Strong Stratospheric Polar Vortex in March 2020 in Sub-Seasonal to Seasonal Models: Implications for Empirical Prediction of the Low Arctic Total Ozone Extreme. *J. Geophys. Res. Atmos.* **2021**, *126*, e2020JD034190. [CrossRef]

34. Marsing, A.; Jurkat-Witschas, T.; Grooß, J.-U.; Kaufmann, S.; Heller, R.; Engel, A.; Hoor, P.; Krause, J.; Voigt, C. Chlorine partitioning in the lowermost Arctic vortex during the cold winter 2015/2016. *Atmos. Chem. Phys.* **2019**, *19*, 10757–10772.

35. Drdla, K.; Müller, R. Temperature thresholds for chlorine activation and ozone loss in the polar stratosphere. *Ann. Geophys.* **2012**, *30*, 1055–1073.

36. Pitts, M.C.; Poole, L.R.; Thomason, L.W. CALIPSO polar stratospheric cloud observations: Second-generation detection algorithm and composition discrimination. *Atmos. Chem. Phys.* **2009**, *9*, 7577–7589. [CrossRef]

37. Spang, R.; Hoffmann, L.; Müller, R.; Grooß, J.-U.; Tritscher, I.; Höpfner, M.; Pitts, M.; Orr, A.; Riese, M. A climatology of polar stratospheric cloud composition between 2002 and 2012 based on MIPAS/Envisat observations. *Atmos. Chem. Phys.* **2018**, *18*, 5089–5113.

38. Kirner, O.; Müller, R.; Ruhnke, R.; Fischer, H. Contribution of liquid, NAT and ice particles to chlorine activation and ozone depletion in Antarctic winter and spring. *Atmos. Chem. Phys.* **2015**, *15*, 2019–2030. [CrossRef]

39. von der Gathen, P.; Kivi, R.; Wohltmann, I.; Salawitch, R.J.; Rex, M. Climate change favours large seasonal loss of Arctic ozone. *Nat. Commun.* **2021**, *12*, 3886.

40. Salawitch, R.J.; Gobbi, G.P.; Wofsy, S.C.; McElroy, M.B. Denitrification in the Antarctic stratosphere. *Nature* **1989**, *339*, 525–527. [CrossRef]

41. Arblaster, J.M.; Gillett, N.P.; Calvo, N.; Forster, P.; Polvani, L.; Son, W.; Waugh, D.; Young, P.; Barnes, E.; Cionni, I. Stratospheric ozone changes and climate. In *Scientific Assessment of Ozone Depletion: 2014*; World Meteorological Organization: Geneva, Switzerland, 2014.

42. Pan, C.; Zhu, B.; Gao, J.; Hou, X.; Kang, H.; Wang, D. Quantifying Arctic lower stratospheric ozone sources in winter and spring. *Sci. Rep.* **2018**, *8*, 8934. [CrossRef]

43. Dobson, G.M.B. Forty years' research on atmospheric ozone at Oxford: A history. *Appl. Opt.* **1968**, *7*, 387–405. [CrossRef] [PubMed]

44. Brewer, A. A replacement for the Dobson spectrophotometer? *Pure Appl. Geophys.* **1973**, *106*, 919–927. [CrossRef]

45. Solomon, S.; Mount, G.H.; Sanders, R.W.; Schmeltekopf, A.L. Visible spectroscopy at McMurdo Station, Antarctica: 2. Observations of OClO. *J. Geophys. Res. Atmos.* **1987**, *92*, 8329–8338. [CrossRef]

46. Logan, J.A. Trends in the vertical distribution of ozone: An analysis of ozonesonde data. *J. Geophys. Res. Atmos.* **1994**, *99*, 25553–25585.

47. Thompson, A.M.; Oltmans, S.J.; Tarasick, D.W.; von der Gathen, P.; Smit, H.G.; Witte, J.C. Strategic ozone sounding networks: Review of design and accomplishments. *Atmos. Environ.* **2011**, *45*, 2145–2163.

48. Wohltmann, I.; von der Gathen, P.; Lehmann, R.; Maturilli, M.; Deckelmann, H.; Manney, G.L.; Davies, J.; Tarasick, D.; Jepsen, N.; Kivi, R. Near-complete local reduction of Arctic stratospheric ozone by severe chemical loss in spring 2020. *Geophys. Res. Lett.* **2020**, *47*, e2020GL089547. [CrossRef]

49. Kuttippurath, J.; Godin-Beekmann, S.; Lefèvre, F.; Nikulin, G.; Santee, M.; Froidevaux, L. Record-breaking ozone loss in the Arctic winter 2010/2011: Comparison with 1996/1997. *Atmos. Chem. Phys.* **2012**, *12*, 7073–7085. [CrossRef]

50. Lu, L.; Bian, L.; Xiao, C. A study on polar atmospheric sciences and global change. *J. Appl. Meteorol. Sci.* **2006**, *17*, 743–755.

51. Platt, U.; Stutz, J. *Differential Optical Absorption Spectroscopy: Principles and Applications*; Springer: Berlin/Heidelberg, Germany, 2008; p. 568.

52. Hüneke, T.; Aderhold, O.-A.; Bounin, J.; Dorf, M.; Gentry, E.; Grossmann, K.; Grooß, J.-U.; Hoor, P.; Jöckel, P.; Kenntner, M. The novel HALO mini-DOAS instrument: Inferring trace gas concentrations from airborne UV/visible limb spectroscopy under all skies using the scaling method. *Atmos. Meas. Tech.* **2017**, *10*, 4209–4234.

53. Frieß, U.; Kreher, K.; Johnston, P.; Platt, U. Ground-based DOAS measurements of stratospheric trace gases at two Antarctic stations during the 2002 ozone hole period. *J. Atmos. Sci.* **2005**, *62*, 765–777. [CrossRef]

54. Bogumil, K.; Orphal, J.; Homann, T.; Voigt, S.; Spietz, P.; Fleischmann, O.; Vogel, A.; Hartmann, M.; Kromminga, H.; Bovensmann, H. Measurements of molecular absorption spectra with the SCIAMACHY pre-flight model: Instrument characterization and reference data for atmospheric remote-sensing in the 230–2380 nm region. *J. Photochem. Photobiol. A Chem.* **2003**, *157*, 167–184. [CrossRef]

55. Hermans, C.; Vandaele, A.; Fally, S.; Carleer, M.; Colin, R.; Coquart, B.; Jenouvrier, A.; Merienne, M.F. Absorption cross-section of the collision-induced bands of oxygen from the UV to the NIR. In *Weakly Interacting Molecular Pairs: Unconventional Absorbers of Radiation in the Atmosphere*; Springer: Berlin/Heidelberg, Germany, 2003; pp. 193–202.

56. Vandaele, A.C.; Hermans, C.; Simon, P.C.; Van Roozendael, M.; Guilmot, J.M.; Carleer, M.; Colin, R. Fourier transform measurement of NO_2 absorption cross-section in the visible range at room temperature. *J. Atmos. Chem.* **1996**, *25*, 289–305. [CrossRef]

57. Bhartia, P.K. OMI Algorithm Theoretical Basis Document Volume II. In *OMI Ozone*; NASA: Washington, DC, USA, 2002.

58. Koukouli, M.E.; Clarisse, L.; Carboni, E.; van Gent, J.; Spinetti, C.; Balis, D.; Dimopoulos, S.; Grainger, D.; Theys, N.; Tampellini, L. Intercomparison of Metop-A SO_2 measure-ments during the 2010-2011 Icelandic eruptions. *Ann. Geophys.* **2014**, *57*, 2110.

59. Kerr, J. New methodology for deriving total ozone and other atmospheric variables from Brewer spectrophotometer direct sun spectra. *J. Geophys. Res. Atmos.* **2002**, *107*, 4731. [CrossRef]

60. Pommereau, J.P.; Goutail, F. O_3 and NO_2 ground-based measurements by visible spectrometry during Arctic winter and spring 1988. *Geophys. Res. Lett.* **1988**, *15*, 891–894. [CrossRef]

61. Hendrick, F.; Pommereau, J.P.; Goutail, F.; Evans, R.D.; Ionov, D.; Pazmino, A.; Kyro, E.; Held, G.; Eriksen, P.; Dorokhov, V.; et al. NDACC/SAOZ UV-visible total ozone measurements: Improved retrieval and comparison with correlative ground-based and satellite observations. *Atmos. Chem. Phys.* **2011**, *11*, 5975–5995. [CrossRef]

62. Bernet, L.; Svendby, T.; Hansen, G.; Orsolini, Y.; Dahlback, A.; Goutail, F.; Pazmiño, A.; Petkov, B.; Kylling, A. Total ozone trends at three northern high-latitude stations. *Atmos. Chem. Phys.* **2023**, *23*, 4165–4184.

63. Zhao, X.; Fioletov, V.; Brohart, M.; Savastiouk, V.; Abboud, I.; Ogyu, A.; Davies, J.; Sit, R.; Lee, S.C.; Cede, A. The world Brewer reference triad–updated performance assessment and new double triad. *Atmos. Meas. Tech.* **2021**, *14*, 2261–2283. [CrossRef]

64. Verhoelst, T.; Granville, J.; Hendrick, F.; Köhler, U.; Lerot, C.; Pommereau, J.-P.; Redondas, A.; Van Roozendael, M.; Lambert, J.-C. Metrology of ground-based satellite validation: Co-location mismatch and smoothing issues of total ozone comparisons. *Atmos. Meas. Tech.* **2015**, *8*, 5039–5062. [CrossRef]

65. Garane, K.; Koukouli, M.-E.; Verhoelst, T.; Lerot, C.; Heue, K.-P.; Fioletov, V.; Balis, D.; Bais, A.; Bazureau, A.; Dehn, A. TROPOMI/S5P total ozone column data: Global ground-based validation and consistency with other satellite missions. *Atmos. Meas. Tech.* **2019**, *12*, 5263–5287. [CrossRef]

66. Solomon, S.; Haskins, J.; Ivy, D.J.; Min, F. Fundamental differences between Arctic and Antarctic ozone depletion. *Proc. Natl. Acad. Sci. USA* **2014**, *111*, 6220–6225. [CrossRef] [PubMed]

67. Wohltmann, I.; von der Gathen, P.; Lehmann, R.; Deckelmann, H.; Manney, G.; Davies, J.; Tarasick, D.; Jepsen, N.; Kivi, R.; Lyall, N. Chemical evolution of the exceptional Arctic stratospheric winter 2019/2020 compared to previous Arctic and Antarctic winters. *J. Geophys. Res. Atmos.* **2021**, *126*, e2020JD034356. [CrossRef]